

# First-principles study of stability of helium-vacancy complexes below tungsten surfaces

Cite as: J. Appl. Phys. **123**, 205108 (2018); <https://doi.org/10.1063/1.5027088>

Submitted: 27 February 2018 . Accepted: 08 May 2018 . Published Online: 24 May 2018

L. Yang, Z. J. Bergstrom, and B. D. Wirth



View Online



Export Citation



CrossMark

## ARTICLES YOU MAY BE INTERESTED IN

[Energetics of hydrogen and helium-vacancy complexes in bulk and near surfaces of tungsten: First-principles study](#)

Journal of Applied Physics **123**, 215104 (2018); <https://doi.org/10.1063/1.5027805>

[Helium segregation and transport behavior near  \$\langle 100 \rangle\$  and  \$\langle 110 \rangle\$  symmetric tilt grain boundaries in tungsten](#)

Journal of Applied Physics **123**, 225104 (2018); <https://doi.org/10.1063/1.5026617>

[A tungsten-rhenium interatomic potential for point defect studies](#)

Journal of Applied Physics **123**, 205102 (2018); <https://doi.org/10.1063/1.5030113>

## Lock-in Amplifiers up to 600 MHz

starting at

\$6,210



Zurich Instruments

Watch the Video



# First-principles study of stability of helium-vacancy complexes below tungsten surfaces

L. Yang,<sup>1,a)</sup> Z. J. Bergstrom,<sup>1</sup> and B. D. Wirth<sup>1,2</sup>

<sup>1</sup>Department of Nuclear Engineering, University of Tennessee, Knoxville, Tennessee 37996, USA

<sup>2</sup>Fusion and Materials for Nuclear Systems Division, Oak Ridge National Laboratory, Oak Ridge, Tennessee 37831, USA

(Received 27 February 2018; accepted 8 May 2018; published online 24 May 2018)

Density function theory calculations have been performed to study the stability of small helium-vacancy (He-V) complexes near tungsten (W) surfaces of different orientations. The results show that the stability of vacancies and He-V complexes near W surfaces depends on surface orientation. However, as the depth below the surface increased beyond about 0.65–0.8 nm, the stability of He-V complexes is similar to the bulk. The formation energies of single vacancies and di-vacancies at depths less than 0.2 nm below the W(110) surface are higher than for W(100) or W(111) surfaces, but have lower energies at depths between 0.2 and 0.65 nm. The formation energies of He-V complexes below W surfaces are sensitive to the geometric orientation of the He and vacancy, especially below the W(111) surface. Within about 0.2 nm of the top layer of the three W surfaces, neither a vacancy nor a di-vacancy can trap He. Because of the lower formation energy of He-V complexes and higher He binding energy to vacancies below the W(110) surface, the He desorption from the W(110) surface is less likely to occur than from the W(100) and W(111) surfaces. Our results provide fundamental insight into the differences in surface morphology changes observed in single W crystals with different surface orientations under He plasma exposure. Published by AIP Publishing. <https://doi.org/10.1063/1.5027088>

## I. INTRODUCTION

The development of a viable, energy-producing fusion reactor faces many issues: one of the most significant of which is the materials challenge that results from the plasma-material interactions (PMI) at the divertor, for which tungsten (W) is the prime candidate because of its high thermal conductivity and melting point, low tritium retention, and low sputtering threshold.<sup>1</sup> Within the International Thermonuclear Experimental Reactor (ITER) device, the divertor plasma-facing materials are expected to experience massive heat loads ( $10\text{--}20\text{ MW m}^{-2}$ ) and particle fluxes ( $10^{24}\text{ m}^{-2}\text{ s}^{-1}$ ) that can cause significant microstructural and morphological changes.<sup>2</sup> The tungsten at the divertor is expected to undergo surface roughening and the formation of a tendril-like fuzz when irradiated with low energy helium (He) ions within the temperature range of 1000–2000 K.<sup>3,4</sup> The formation of this fuzz and other damage effects is concerning because this may lead to enhanced erosion, limiting the life of components as well as being a source for radioactive, tritium-containing dust, and possible enhanced tritium retention increasing fuel costs.<sup>5–8</sup> In order to gain insight into the formation mechanism of nanofuzz growth in fusion-plasma-facing W, many investigations have been conducted on the He behavior near W surfaces as well as the effect of He implantation on the microstructure of W surfaces.<sup>9–20</sup>

Experimental studies have indicated that bubble formation and surface morphology are influenced by surface orientations under He plasma exposure.<sup>17–20</sup> Yamagiwa *et al.*<sup>17</sup>

investigated the difference in He bubble formation and the morphology change of three types of W samples due to He plasma exposure by scanning electron microscopy (SEM), scanning ion microscopy (SIM), and transition electron microscopy (TEM). The non-uniformity of the formation of He bubbles within a depth of  $1\text{ }\mu\text{m}$  below surfaces was observed on ITER grade W, which might be caused by the difference in the orientation of the crystal grains. Moreover, they found that the less damaged surface had a (110) orientation. After low energy He plasma exposure, a clear difference in the surface morphology was also observed on crystal grains of different surfaces by Ohno *et al.*<sup>18</sup> The work of Parish *et al.*<sup>19</sup> shows that low energy He plasma resulted in roughening and surface morphology changes to smooth-polished W. Furthermore, four different surface morphologies were observed, including smooth, pyramidal, wavy, and terraced, and these different surface responses were correlated with surface orientation. Kajita *et al.*<sup>20</sup> investigated the surface morphology changes due to He plasma irradiation on single crystal W samples and observed differences in surface morphology changes between (100) and (110) single crystal tungsten samples when the He fluence was less than  $10^{25}\text{ m}^{-2}$ . Protrusions were formed on the W (100) surface, presumably due to the bursting of He bubbles, while wavy structures with a height of  $\sim 200\text{ nm}$  containing sub-surface He bubbles cover the W(110) surface. Moreover, it was found that the density of He bubbles below the W(110) surface is less than the W(100) case.

Besides experimental studies, computer simulations have been employed to explore the He behavior near W surfaces. Because of the insolubility of He in W, He has a

<sup>a)</sup> Author to whom correspondence should be addressed: liyang@utk.edu

strong driving force to self-cluster and will also be trapped at vacancies or other defects. Upon reaching a critical interstitial He cluster size that varies from about eight He in the bulk to as small as two He near surfaces, trap mutation (TM) occurs in which a lattice atom is displaced from its site creating a W Frenkel pair.<sup>21</sup> Molecular dynamics (MD) simulations on the motion of small mobile He clusters near W surfaces demonstrate that TM is activated at rates higher than in the bulk. Moreover, TM produces W adatoms and immobile He-vacancy (He-V) complexes at a short distance from the surface layer.<sup>22</sup> These He-V complexes will continue to accumulate He and grow by trap mutation or loop-punching.<sup>23</sup> The dissolution, self-trapping, and clustering of He at W surfaces have been investigated by using a first-principles method based on the density functional theory (DFT),<sup>24,25</sup> and it was found that the vacancy and the He-V complex are able to form near the surface due to He accumulation and the TM mechanism, and that accumulation is dependent on surface orientation. In addition, He-V complexes near W surfaces could be produced through He trapping by pre-existing vacancy clusters under the implantation of high fluxes of He ions and neutron irradiation in a fusion environment. Pan *et al.*<sup>25</sup> studied the single vacancy formation at the W surfaces with different orientations; however, the number of atomic layers investigated was limited due to the small models of surface slabs, which limits information between the surface layers and the bulk. Moreover, the energetics of vacancy clusters and He-V complexes near W surfaces are not available in the current literature. In this work, based on large surface slab models, we have calculated the formation energies of single vacancy, di-vacancy, and He<sub>m</sub>V<sub>n</sub> ( $m = 0-3$ ,  $n = 0-2$ ) complexes, as well as He binding energies, as a function of distance below W(100), W(110), and W(111) surfaces using DFT, and analyzed the stability of He-V complexes near these three W surfaces. This study is helpful not only for understanding the early stages of He bubble formation near W surfaces but also for providing a database of W-He interactions that can accurately describe the response of W surfaces to He irradiation.

## II. METHODOLOGY

The Vienna Ab initio Simulation Package (VASP),<sup>26</sup> along with the standard pseudopotentials of He and W, was used in this work. The interaction between ions and electrons was described by the projector-augmented wave method,<sup>27,28</sup> while exchange and correlation interactions were obtained by the generalized gradient approximation in the Perdew-Burke-Ernzerhof form.<sup>29</sup> The energy cutoff for the plane-wave basis set was set as 360 eV. The first-order Methfessel-Paxton method was applied for the Fermi surface smearing with a width of 0.1 eV. The Monkhorst-Pack scheme was used to sample the Brillouin zone (BZ) and generate k-point grids.

A cubic bcc supercell with  $4a \times 4a \times 4a$ , where  $a$  is the lattice constant of 0.3171 nm, was employed to get the energetics of ground state configurations of He-V complexes in bulk W. A slab geometry was used to model W surfaces, which includes multi W atom layers and a 1.2 nm vacuum

layer. The W(100), W(110), and W(111) surfaces contain 16, 12, and 24 atom layers, respectively. The bottom three layers of the W(100) and W(110) as well as the bottom six layers of the W(111) were fixed, while the remaining layers were relaxed freely. The dimensions of the simulation models and the number of W atoms for bulk and the three W surfaces are listed in Table I. A reconstruction model was employed for the W(100) surface, in which the top layer atoms shift 0.027 nm and the second layer atoms shift 0.004 nm to form zigzag chains.<sup>30</sup> All calculations were performed at constant volume, and using period boundary conditions for three dimensions of bulk W and along the x and y directions of surface models. The convergence criteria for the electronic self-consistent iteration and the force on the unfixed atoms were  $10^{-5}$  eV and 0.01 eV/Å, respectively.

The formation energy of a He<sub>m</sub>V<sub>n</sub> ( $m = 0-3$ ,  $n = 0-2$ ) is given by

$$E_{\text{He}_m\text{V}_n}^f = E_{s+\text{He}_m\text{V}_n}^{\text{tot}} - E_s^{\text{tot}} + nE_W - mE_{\text{He}}, \quad (1)$$

where  $E_{s+\text{He}_m\text{V}_n}^{\text{tot}}$  and  $E_s^{\text{tot}}$  are the total energies of the system with and without a He<sub>m</sub>V<sub>n</sub>,  $E_W$  is the energy per W atom in the bulk supercell,  $E_{\text{He}}$  is the energy of an isolated He, and  $m$  and  $n$  are the number of He and vacancies. The initial configuration of the He<sub>m</sub>V<sub>n</sub> complex below the W surfaces is based on that obtained in bulk W.

In order to explore the di-vacancy stability and the He trapping ability of He-V complexes near W surfaces, the binding energy of di-vacancy and that of a single He to a He-V complex were obtained. The binding energy between A and B is defined as

$$E_{A+B}^b = E_A^f + E_B^f - E_{A+B}^f, \quad (2)$$

where  $E_A^f$ ,  $E_B^f$ , and  $E_{A+B}^f$  are the formation energies of A, B, and A+B, respectively.

## III. RESULTS AND DISCUSSION

Previous MD and molecular statics (MS) simulations illustrate that He atoms are implanted within a depth of a few nm below W surfaces under low-energy helium plasma exposure,<sup>31,32</sup> and the behavior of He near W surfaces is much different from the bulk.<sup>33</sup> The present results show that the surface region below the W(100), W(110), and W(111) surfaces (the depth  $d$  is less than 1.0 nm) can be divided into three regions for the stability of vacancies and small He-V complexes. We define these as region I, in which the surface strongly influences formation and binding

TABLE I. Dimension (nm) of simulation models and number of W atoms for bulk and W(100), W(110), and W(111) surfaces.

Model	Dimension (nm)			No. of W atoms
	x	y	z	
Bulk	1.268	1.268	1.268	128
(100)	1.268	1.268	3.578	256
(110)	1.345	1.268	3.666	288
(111)	1.345	1.553	3.305	288

TABLE II. Formation energy (eV) of a vacancy at different layer depths below W surfaces. \* denotes that a vacancy in L2 below a W(100) surface is unstable.

Structure	k-point	L1	L2	L3	L4	L5	L6	L7	L8	L9	L10
W(100)	$3 \times 3 \times 1$	0.356	*	3.071	3.503	3.407	3.353	3.365			
	$4 \times 4 \times 1$	0.355	*	3.056	3.489	3.346	3.332	3.331			
	$5 \times 5 \times 1$	0.353	*	3.048	3.469	3.331	3.300	3.295			
W(110)	$4 \times 3 \times 1$	1.80	2.94	3.12	3.31	3.29	3.34				
W(111)	$4 \times 4 \times 1$	0.68	1.79	2.73	3.29	3.66	3.41	3.41	3.28	3.37	3.39

energies, then a transition region we define as region II, and finally, with increasing depth, region III where the influence of the surface is diminished and the formation energies approach the bulk values. In this section, we discuss the formation and binding energies of single vacancy, di-vacancy, and He-V complexes in these three regions below W surfaces.

## A. Vacancy and di-vacancy at W surfaces

### 1. Formation energies of a single vacancy

Vacancies at W surfaces can be produced due to high energy particle irradiation, as well as low to intermediate energy plasma exposure. The vacancy formation energies also provide information about the stability of surfaces under irradiation. Previous DFT results show that the value of the vacancy formation energy in bulk W depends on the k-point sampling.<sup>34,35</sup> Thus, to test the effect of the k-point number on the results, the  $3 \times 3 \times 1$ ,  $4 \times 4 \times 1$  or  $5 \times 5 \times 1$  k-point sampling was used in the calculations of vacancy formation energy near the W(100) surface and the results are listed in Table II, where Ln ( $n = 1-10$ ) describe the vacancy formation energy with the vacancy placed within the  $n^{\text{th}}$  atomic layers below the W surface. Table II clearly demonstrates that the vacancy formation energy decreases slightly with increasing number of k-points; moreover, the different k-point samplings have only a minor effect on the relative vacancy formation energies as a function of depth below the W(100) surface. The largest difference in the vacancy formation energy between the  $3 \times 3 \times 1$  and  $4 \times 4 \times 1$  k-point samplings happens at the 5th layer, which is about 1.8%, while the largest difference at the 7th layer is 1.1% between the  $4 \times 4 \times 1$  and  $5 \times 5 \times 1$  k-point samplings. In addition, the vacancy formation energies in bulk W with the same dimensions along the x and y directions are 3.334, 3.330, and 3.257 eV for the k-point samplings of  $3 \times 3 \times 3$ ,  $4 \times 4 \times 4$ , and  $5 \times 5 \times 5$ , respectively. When the depth below the surface is sufficiently large, the formation energy should converge to the bulk value. The values of vacancy formation energy at the 6th and 7th layers below the W(100) surface for the  $4 \times 4 \times 1$  k-point sampling are very close to that in bulk W for the  $4 \times 4 \times 4$  k-point sampling. Based on these analyses and the dimensions of the surfaces (see Table I), the  $4 \times 4 \times 4$ ,  $4 \times 4 \times 1$ ,  $4 \times 4 \times 1$ , and  $4 \times 3 \times 1$  k-point samplings were chosen in the following calculations for bulk W, W(100), W(110), and W(111) surfaces, respectively.

To display the relationship between the vacancy formation energy and the position of the vacancy visually, the data in Table II as a function of depth ( $d$ ) are also shown in

Fig. 1. It is found that the vacancy formation energy at the first layer of the W(100) surface is the lowest, and the vacancy at the 2nd layer of the W(100) surface is unstable and moves up to the first layer after relaxation, similar to Ref. 25. The vacancy formation energies at the top four layers of the W(110) surface are higher than those at the corresponding layers of the W(111) surface. From Table II, one can see that the vacancy formation energies at the 5th, 4th, and 9th layers of the W(100), W(110), and W(111) surfaces, respectively, are close to the bulk value of 3.33 eV. The 5th, 4th, and 9th layers are the critical layers for the stability of the three W surfaces, and these critical layers correspond to the similar depth, about 0.62–0.67 nm (see Fig. 1), which is the boundary between surface regions II and III. With increasing depth, the influence of the surface on the vacancy formation energy is negligible. This implies that the region of influence of a W surface on the vacancy is roughly independent of surface orientation. It is unexpected that the vacancy formation energies near the W(100) and W(111) surfaces do not increase monotonically with depth from the first layer to the critical layer, as shown in Fig. 1. The vacancies at the 4th layer ( $d = 0.47$  nm) below the W(100) surface and the 5th layer ( $d = 0.34$  nm) below the W(111) surface have higher formation energies than in the bulk, which implies that the two layers are more difficult to form vacancies. In addition, the vacancy formation energy at the 8th layer ( $d = 0.61$  nm) below the W(111) surface is lower than

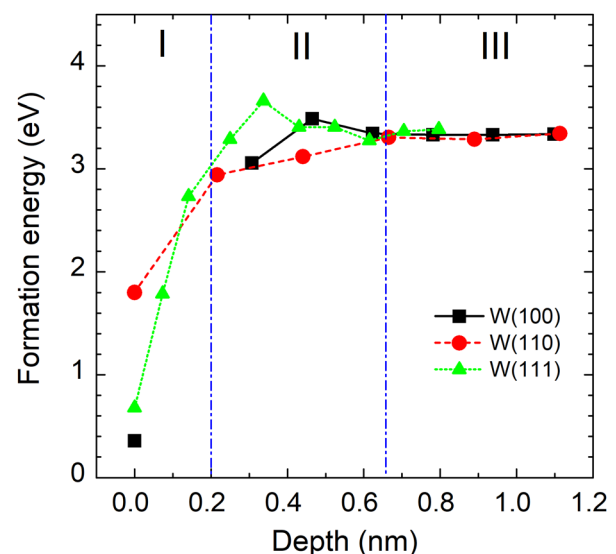


FIG. 1. Formation energies of vacancy as a function of depth below the W(100), W(110), and W(111) surfaces, where I, II, and III represent three regions.

that at its nearest four layers (i.e., L6, L7, L9, and L10). However, the fluctuation of the vacancy formation energies beyond the critical layer (L4) of the W(110) surface was not observed. The particular phenomenon of the vacancy formation near the W(100) and W(111) surfaces should be attributed to the surface reconstruction, resulting in distinctive electron distributions. Except for the slight fluctuation, the vacancy formation energies near the three W surfaces roughly increase with depths beyond the critical layer. Figure 1 shows that the surface region below the W(100), W(110), and W(111) surfaces can be divided into three regions. In the first near surface region (region I,  $d < 0.2$  nm), the surface strongly influences the vacancy formation energy. In this region, the influence of the W(110) surface is weaker than the W(100) and W(111) surfaces, resulting in a higher vacancy formation energy below the W(110) surface. Within the second near surface region (region II,  $0.2$  nm  $< d < 0.65$  nm), the vacancy formation energy below the W(110) surface is lower than the other two surfaces. In region III ( $d > 0.65$  nm), the vacancy formation energy approaches to the bulk value.

## 2. Di-vacancy formation and binding energies

It is known that in bulk W the formation energy of a di-vacancy at the first nearest-neighbor (1NN) positions is similar to that at the third NN (3NN) positions, but about 0.35 eV lower than that at the second NN (2NN) positions.<sup>35</sup> Here, we mainly focus on the formation energy of the 1NN di-vacancy ( $V_{2-1NN}$ ) near the three W surfaces as a function of depth of the di-vacancy center, which are plotted in Fig. 2. To probe the stability of the top layers of W surfaces with different surface orientations, the 2NN and 3NN di-vacancies ( $V_{2-2NN}$

and  $V_{2-3NN}$ ) on the surface layers of the W(100) and W(111) surfaces, respectively, were also investigated. Note that the definitions of the 1NN, 2NN, and 3NN di-vacancies in this work were based on the distance of neighbor lattice sites in bulk W. The  $V_{2-1NN}$  near the W(100) surface is located at the two nearest atomic layers. For the three top layers of the W(100) surface, the stability of the  $V_{2-1NN}$  depends on the vacancy orientation due to the surface reconstruction with zigzag chains. In Fig. 2, the formation energies of the  $V_{2-1NN}$  near the W(100) surface correspond to the configurations with minimum energies, which might distribute along different  $\langle 111 \rangle$  directions. It should be noted that the  $V_{2-2NN}$  at the W(100) surface layer has the lowest formation energy of 0.56 eV, which further confirms that the W(100) surface layer is more easily damaged. The  $V_{2-2NN}$  at the 2nd layer below the W(100) surface is unstable, as illustrated in Fig. 3. After relaxation, one atom on the top layer moves to a vacant site on the 2nd layer by a first nearest neighbor exchange, which is the same as the single vacancy on the 2nd layer below the W(100) surface. However, another two atoms on the surface layer displace about 0.1 nm towards the other vacancy on the 2nd layer, resulting in the collapse of the W(100) surface layer. For the W(100) and W(110) surfaces, the formation energies of  $V_{2-1NN}$  increase with depth until about 0.65 nm below the surface. The  $V_{2-1NN}$  near the W(111) surface has two configurations: one is that the two vacancies are along the  $[111]$  direction, perpendicular to the surface layer; the other is that the  $V_{2-1NN}$  is along the non- $[111]$  direction, including the  $[1\bar{1}1]$ ,  $[\bar{1}11]$ , and  $[11\bar{1}]$  directions. The formation energies of the  $V_{2-1NN}$  along the three non- $[111]$  directions at the same depth are identical. It is obvious that near

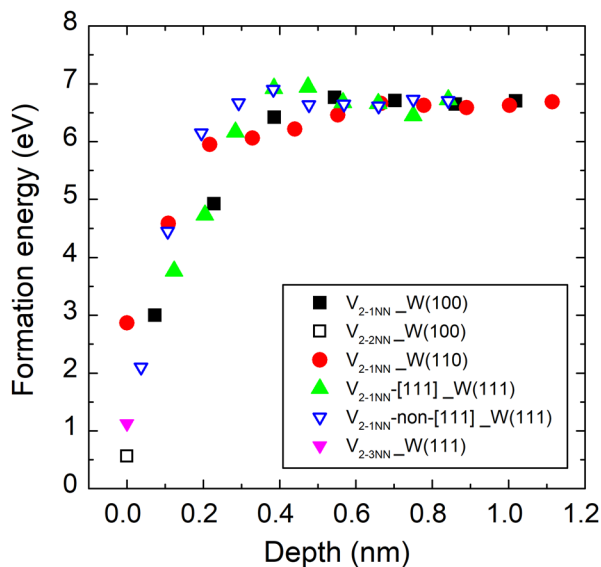


FIG. 2. Formation energies of di-vacancies as a function of depth below the W(100), W(110), and W(111) surfaces, where the black full and hollow squares represent the 1NN and 2NN di-vacancies at the W(100) surface, the red spheres represent the 1NN di-vacancies at the W(110) surface, the green filled and blue hollow triangles indicate the 1NN di-vacancies along the  $[111]$  and non- $[111]$  directions at the W(111) surface, and the magenta filled triangle represents the 3NN di-vacancy at the surface layer of the W(111) surface.

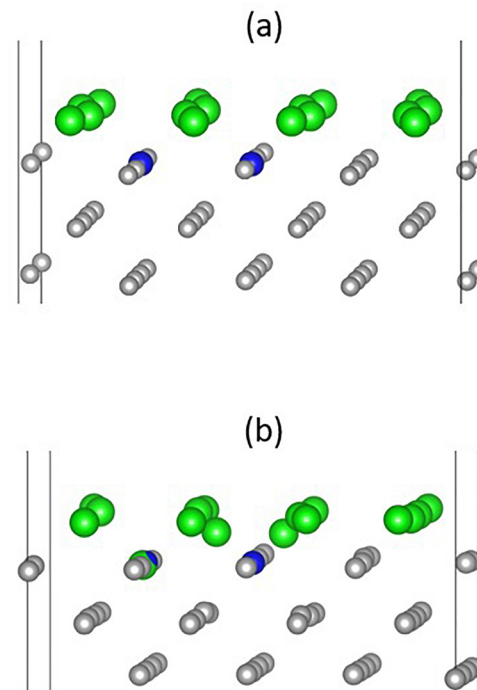


FIG. 3. (a) Initial and (b) final configuration of a  $V_{2-2nn}$  on the 2nd layer below the W(100) surface. Green and grey spheres represent the W atoms on the top layer and below the surface, respectively, in the initial configuration. The blue spheres illustrate the di-vacancy.

the W(111) surface, the formation energies of the  $V_{2-1NN}$  along the [111] direction at depths less than 0.4 nm are lower than that of the non-[111] directions at similar depths, which suggests that the di-vacancy perpendicular to the surface is more energetically favorable. For depths from 0.4 to 0.8 nm below the W(111) surface, the formation energy of the  $V_{2-1NN}$  trends toward a constant value essentially independent of vacancy orientation and depth. It can be seen from Fig. 2 that for depths less than 0.4 nm, the formation energies of the  $V_{2-1NN}$  significantly decrease approaching the surface, but approach a constant value for depths beyond 0.65 nm for the three W surfaces investigated. The three regions near the three W surfaces for the di-vacancy formation energies are similar to that for the formation energies of single vacancies. The di-vacancy formation energies near the W(110) surface are the largest when the depth is less than 0.2 nm, but the lowest for depths between 0.2 and 0.65 nm. Beyond 0.65 nm, all of them approach the bulk value of 6.7 eV.

Based on the formation energies of the single vacancy and the di-vacancy, the di-vacancy binding energies near the W(100), W(110), and W(111) surfaces can also be assessed. Previous DFT results demonstrate that di-vacancies at either the first or second NN positions in bulk W are unstable, with a strong repulsion observed especially for the 2NN configuration.<sup>35,36</sup> As illustrated in Fig. 4, numerous bound di-vacancy configurations are observed near W surfaces. For example, the binding energy of the  $V_{2-2NN}$  at the surface layer of the W(100) is 0.15 eV, indicating the attractive interaction between the two vacancies. Besides the  $V_{2-2NN}$  on the surface layer, the positive binding energies of the  $V_{2-1NN}$  are obtained at the 3rd-4th layers (the two vacancies are located at the 3rd and 4th layers, respectively,  $d=0.386$  nm) and the 4th-5th layers ( $d=0.544$  nm) below the W(100) surface. For the case of the W(110) surface, the  $V_{2-1NN}$  at the surface layer is very stable with a high binding energy of 0.74 eV; however, the di-vacancy binding energy decreases steeply with

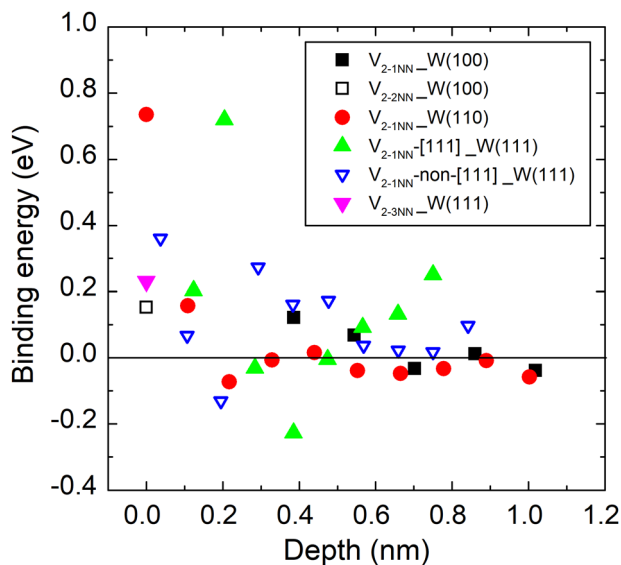


FIG. 4. Di-vacancy binding energies as a function of depth near the W(100), W(110), and W(111) surfaces, where the representations of the symbols are the same as those in Fig. 2.

increasing depth below the surface. For depths larger than 0.2 nm, the binding energy is around 0 eV. The  $V_{2-3NN}$  on the surface layer and most of  $V_{2-1NN}$  near the W(111) surface have positive binding energies. For depths less than 0.8 nm, the di-vacancy binding energies near the W(111) fluctuate more significantly with increasing depth than below the W(100) and W(110) surfaces, respectively. At a depth of 0.2 nm (the 2nd-5th layers) below the W(111) surface, the  $V_{2-1NN}$  along the [111] direction combine strongly with a binding energy of 0.72 eV. However, the  $V_{2-1NN}$  along the non-[111] direction at the 3rd-4th layers ( $d=0.2$  nm) of the W(111) surface is unstable with a negative binding energy, as shown in Fig. 4, which should be attributed to the surface reconstruction with a triple pattern, i.e., the top three layers move toward each other and the layer space between the 3rd and 4th layers expands significantly.<sup>37</sup> Furthermore, the di-vacancy along the [111] direction at a depth of 0.385 nm (the 4–7th layers) below the W(111) surface has the lowest binding energy and is thus the most unstable. In general, the di-vacancy binding energies for the three W surfaces converge as the depth increases beyond 0.8 nm. Low formation energies and high binding energies of vacancies near the surfaces indicate a W surface instability against topological disorder during particle irradiation.

## B. Stability of $He_mV_n$ complexes at W surfaces

$He_mV_n$  complexes near a W surface might form by two mechanisms. One is that the  $He_n$  are trapped by pre-existing near surface vacancies, and the other is that small mobile  $He_n$  clusters induce TM reactions near surfaces and occupy the lattice sites, forming a  $He_mV_n$  complex, as has been observed in DFT and MD simulations.<sup>22–25</sup> No matter the formation pathway, the formation energy of  $He_mV_n$ , and the binding energy of He to  $He_{m-1}V_n$  clusters are required to understand the stability of  $He_mV_n$  complexes near W surfaces. In this work, small  $He_mV_n$  ( $m=1, 2, 3, n=1, 2$ ) complexes are considered as a function of depth below the W(100), W(110), or W(111) surface.

### 1. $He_mV$ ( $m=1, 2, 3$ )

The formation energy of a substitutional He ( $HeV$  for short) at different layer depths below the three W surfaces is displayed in Table III. The formation energies of a  $HeV$  at the two top layers of the W(100) and W(111) surfaces, as well as at the first layer of the W(110) surface, are not presented in Table III. This is because the He is not stably trapped by the vacancies at these locations, desorbing from the surface. In other words, under the 3rd layer of the

TABLE III. Formation energy (eV) of a substitutional He at different layer depths below W surfaces. \* denotes that helium was unstable and desorbed.

Structure	L1	L2	L3	L4	L5	L6	L7	L8	L9	L10
W(100)	*	*	4.68	5.12	4.95	4.97	4.94			
W(110)	*	4.66	4.69	4.92	4.89	4.95				
W(111)	*	*	4.16	5.16	5.30	5.00	5.02	4.88	5.00	5.02

W(100) and W(111) surfaces, and the 2nd layer of the W(110) surface, the He can be trapped by the vacancies. However, the formation energies of HeV at the same layer below the three surfaces are different. With the exception of the HeV at the 3rd layer below the W(111), the HeV has lower formation energies near the W(110) surface than the other two surfaces.

In addition to the HeV, the configurations and stability of the He<sub>2</sub>V at different depths below the W(100), W(110), and W(111) surfaces were investigated. Based on the stability of HeV near W surfaces, the 1st layers of the W(100), W(110), and W(111) as well as the 2nd layers of the W(100) and W(111) were not considered for the He<sub>2</sub>V. In bulk W,

the ground state of a He<sub>2</sub>V has a  $\langle 111 \rangle$  dumbbell-like configuration. Therefore, four initial possible  $\langle 111 \rangle$  dumbbell configurations, i.e.,  $[111]$ ,  $[11\bar{1}]$ ,  $[1\bar{1}1]$ , and  $[1\bar{1}\bar{1}]$  dumbbells, were first considered at the top few layers below the three W surfaces. As well, initial  $\langle 100 \rangle$  and  $\langle 110 \rangle$  dumbbell-like He<sub>2</sub>V configurations were also explored at the top stable layer. After relaxation, the most stable configurations of He<sub>2</sub>V at different layers of the W(100) surface are still  $\langle 111 \rangle$  dumbbells; however, the orientation of the He<sub>2</sub>V at the 3rd and 4th layers are special, as shown in Fig. 5. It is interesting to see that both the top He (closer to the surface) of the most stable He<sub>2</sub>V at the two layers, as indicated by the larger red and blue spheres, are closer to the long bridge sites [stars in

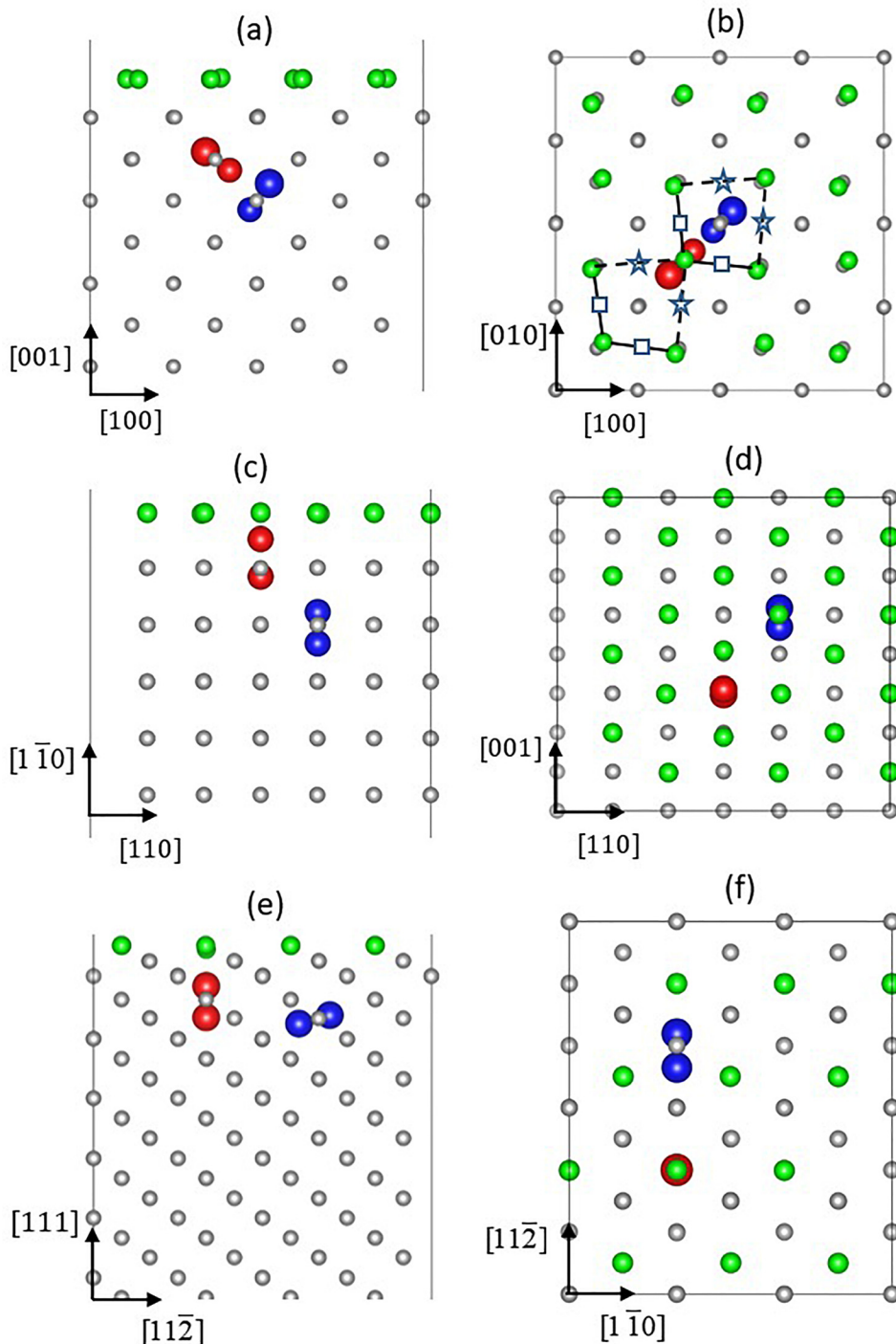


FIG. 5. Configurations of the stable He<sub>2</sub>V as viewed from the (a) side and (b) top of the W(100) surface; (c) side and (d) top of the W(110) surface; and (e) side and (f) top of the W(111) surface. In (a), (c), and (e), only the top parts of surfaces are displayed for clarify. The green and grey spheres represent the W atoms on the top layer and below the surface, respectively. The red and blue spheres represent the He atoms at different layers. The stars and the squares in (b) demonstrate the long and short bridge sites on the W(100) surface.

Fig. 5(b)]; however, this special He orientation essentially vanishes at the 5th layer below the W(100) surface.

For the case of the W(110) surface, the most stable configurations of  $\text{He}_2\text{V}$  at the 2nd and 3rd layer depths are illustrated in Figs. 5(c) (side view) and 5(d) (top view). At the 2nd layer, the  $\text{He}_2\text{V}$  is aligned along the  $[1\bar{1}0]$  direction, and the mass center moves towards the surface, forming a configuration most appropriately described as a HeV and an interstitial He. For depths beyond the 2nd layer below the (110) surface, the  $\langle 111 \rangle$  dumbbell-like configuration is the most stable for  $\text{He}_2\text{V}$ . However, there are two types of  $\langle 111 \rangle$  dumbbells for the  $\text{He}_2\text{V}$  near the W(110) surface. The first has two He along the  $[111]$  or  $[11\bar{1}]$  direction located at the same atomic layer [i.e., on the  $(1\bar{1}0)$  plane], and the second has two He across an atomic layer [i.e., on the (110) plane]. The latter is shown by the blue spheres in Fig. 5(c). At the 3rd layer below the surface, the  $\text{He}_2\text{V}$  prefers to stay on the (110) plane, with an energy that is 0.05 eV lower than that on the  $(1\bar{1}0)$  plane. Beyond the 5th layer below the W(110) surface, the orientation dependence of the  $\langle 111 \rangle$  dumbbell  $\text{He}_2\text{V}$  can be ignored.

For the case of the W(111) surface, the  $\text{He}_2\text{V}$  on the 3rd layer is unstable, which indicates that the vacancy on the 3rd layer of the W(111) can only trap one He. For the stable  $\text{He}_2\text{V}$  near the W(111) surface, there are two distinct  $\langle 111 \rangle$  dumbbells, including the  $[111]$  direction and non- $[111]$  direction. The  $[111]$  direction is the most energetically favorable for the  $\text{He}_2\text{V}$  at the 4th layer, as shown by the red spheres in Figs. 5(e) and 5(f), which has 0.11 eV lower formation energy than the other  $\langle 111 \rangle$  dumbbells. However, the  $\text{He}_2\text{V}$  at the 5th layer has a 0.11 eV lower formation energy in the non- $[111]$  direction relative to the  $[111]$  direction, as indicated by the blue spheres in Figs. 5(e) and 5(f). The  $\text{He}_2\text{V}$  at the 6th and 8th layers has the same favorite direction as that at the 4th layer, while the  $\text{He}_2\text{V}$  at the 7th and

9th layers has the same direction as that at the 5th layer, even though the He orientation dependence of the formation energy decreases with increasing depth.

It is known that He has a closed-shell electronic structure and prefers larger volumes with reduced electron density; therefore, vacancies and vacancy clusters, edge dislocation cores, surfaces, and grain boundaries act as trapping sinks for He,<sup>33,38–40</sup> and the modified formation and binding energies near surfaces are thus a manifestation of this effect. Due to surface attraction, interstitial He or mobile He-V complexes below W surfaces will experience a drift force that biases the diffusion towards surfaces.<sup>22,39</sup> For the He-V complex near W surfaces, the geometry orientation of He and vacancies is sensitive to the surface orientation and the depth below the surface, as illustrated in Fig. 5. To understand the geometric orientation dependence of He-V complexes below W surfaces, as an example, we have investigated the charge density distribution on the  $(1\bar{1}0)$  plane near a  $\text{He}_2\text{V}$  at the 3rd or 4th layer below the W(100) surface, as shown in Fig. 6, where “A” to “H” represent W atoms, and “He<sub>1</sub>” and “He<sub>2</sub>” indicate the two He atoms. Figure 6(a) shows that the two He in a vacancy at the 3rd layer are aligned in the  $[\bar{1}\bar{1}1]$  direction. The W atoms on the W(100) surface layer displace about 0.027 nm along the  $[110]$  direction due to the reconstruction, leading to an asymmetry of the charge density distribution between the first nearest neighbor W atoms, especially for the atoms on the top few layers, as shown in Fig. 6. If there is only one He in the vacancy at the 3rd or 4th layer, it would occupy the vacancy because the trapping ability of the vacancy to He is competitive with the surface to He. However, one He in the  $\text{He}_2\text{V}$  is trying to occupy the vacancy, and the other He is trying to desorb from the surface. Moreover, the charge between atom “B” and “C” is much weaker than that between “A” and “C” or between “B” and “D,” which

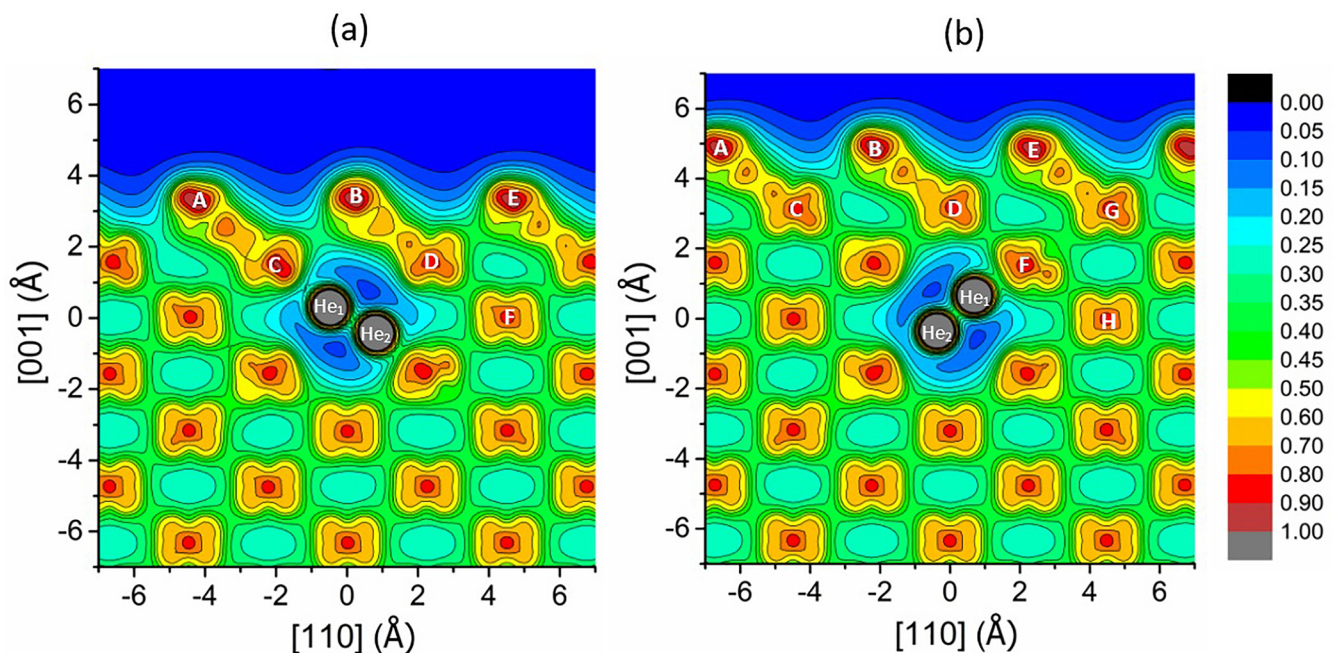


FIG. 6. Charge density ( $e/\text{Å}^3$ ) distribution on the  $(1\bar{1}0)$  plane near a  $\text{He}_2\text{V}$  at the (a) 3rd and (b) 4th layer below the W(100) surface, respectively.

suggests that He prefers to approach to the charge deficit region between “B” and “C.” However, the strong charge between “B” and “D” forces “He<sub>1</sub>” to rotate anticlockwise and close to atom “C.” Accordingly, the “He<sub>2</sub>” adjusts its position based on the interactions with “He<sub>1</sub>” and its first nearest neighbor W atoms, forming the stable  $[\bar{1}\bar{1}1]$  dumbbell-like He<sub>2</sub>V configuration, as shown in Fig. 6(a). Similarly, one He in the He<sub>2</sub>V at the 4th layer below the W(100) surface is close to “F.” Because of the charge shift of atom “D,” “E,” and “F,” the charge deficit between D and F attracts “He<sub>1</sub>.” In brief, the multifarious orientations of He-V complexes below different W surfaces depend on many factors, such as the trapping competition of the surface and vacancy to He, the local geometric distribution of W atoms (and corresponding charge distribution due to the surface effect), and the interactions between He.

The formation energies of the minimum energy He<sub>2</sub>V at different layers below the W(100), W(110), and W(111) surfaces are presented in Table IV. The formation energy of He<sub>2</sub>V at the 3rd layer below the W(100) surface is lower than in the bulk, but at the 4th layer, it is the highest and is close to the bulk value at the 5th layer. Under the 3rd layer of the W(110) surface, the fluctuation of the formation energy of He<sub>2</sub>V is less than 1%. As described above, the vacancy at the two top layers of the W(111) surface is not stable traps (sinks) for He, while a vacancy at the 3rd layer can trap one He. It is somewhat surprising that the formation energy of the He<sub>2</sub>V is the largest at the 4th layer below the W(111) surface, and increases with proximity to the (111) surface before slowly decreasing towards the bulk value for depths beyond the 5th layer.

In bulk W, three He atoms in the most stable He<sub>3</sub>V share a vacant site, lying on a {111} plane and forming an equilateral triangle. However, the energies of the He<sub>3</sub>V near the W surfaces depend on the He and surface orientation, even though they remain on a {111} plane. The most stable configurations of He<sub>3</sub>V at the 3rd, 4th, and 5th layers below the W(100) surface are shown in Figs. 7(a) and 7(b). For depths below the 5th layer, the He orientation dependence can be ignored since the largest energy difference for the He<sub>3</sub>V at different {111} plane is less than 0.05 eV. The  $\{\bar{1}\bar{1}2\}$  plane is the most energetically favorable for the He<sub>3</sub>V at the 2nd layer of the W(110) surface, as shown in Figs. 7(c) and 7(d), no matter the initial configuration of the He<sub>3</sub>V. However, all {111} planes are equivalent for the He<sub>3</sub>V preferred configuration for depths beyond the 2nd layer under the W(110) surface. The He<sub>3</sub>V is stable in a {111} configuration under the 3rd layers of the W(111) surface, but He<sub>3</sub>V at the 4th and 5th layers prefers a specific (111) plane configuration. Especially, the formation energy of He<sub>3</sub>V at the (111) plane,

as indicated by the red spheres in Figs. 7(e) and 7(f), is 0.55 eV lower than metastable configurations on the other {111} plane. The most stable configurations of He<sub>3</sub>V at the 6th and 7th layers are shown by the blue and black spheres, respectively, in Figs. 7(e) and 7(f). Beyond the 7th layer, the largest energy difference of the He<sub>3</sub>V at different {111} planes is less than 0.1 eV. In general, the W(111) surface effect on the configurations of He-V complexes is more significant than for the W(100) and W(110) surfaces.

The formation energies of the most stable He<sub>3</sub>V at different layers below the W surfaces are listed in Table V. It is clear that the formation energies of He<sub>3</sub>V beyond the 4th layer below the W(100) surface are similar to the bulk value of 11.06 eV, but the He<sub>3</sub>V at the 4th layer has the largest formation energy compared to the other depths. For the case of the W(110) surface, the formation energy of the stable He<sub>3</sub>V increases with depth and approaches the bulk value at the 4th layer. As shown in Table V, the formation energy of the stable He<sub>3</sub>V at the 4th layer below the W(111) surface is the largest and then fluctuates weakly around the bulk value with increasing depth, except for the 8th layer.

The data presented in Tables III–V are plotted in Fig. 8. A comparison of Fig. 8 to Fig. 1 shows that the variation in formation energies of HeV as a function of depth is similar to that of the vacancy at the corresponding surface. With increasing number of He, the relative formation energies of He<sub>m</sub>V at different depths are changed slightly for the W(100) and W(110) surfaces, but dramatically for the W(111) surface. It is of interest to note that the formation energies of He<sub>m</sub>V within the depth of 0.2–0.6 nm below the W(110) surface are lower than that at a similar depth below the W(100) and W(111) surfaces, which indicates that small He-V complexes are most stable in this region near the W(110) surface. Furthermore, the formation energies of He<sub>m</sub>V ( $m = 1, 2, 3$ ) complexes at a depth of about 0.65 nm below the surface converge toward the bulk values for the three W surfaces considered.

To assess the He trapping ability of He-V complexes, the binding energies of He to He<sub>m-1</sub>V complexes were calculated. According to Eq. (2), the formation energy of He, along with the He-V complex, is required to calculate the He binding energy. The He interstitial at the 1st and 2nd layers below the W(100) surface is unstable, but stable for depths beyond the 2nd layer, and these data are shown in Fig. 9. The tetrahedral interstitial sites (TISs) below the W(100) surface were defined based on the bcc W configuration beyond the 2nd layer. It should be pointed out that in Ref. 25, it was observed that He TIS between the 2nd and 3rd layers, and at the 3rd layer are unstable, and induce TM, creating adatoms on the first layer and a HeV. This difference occurs because the initial positions of He in Fig. S5 of Ref. 25 are deviated from the TISs that are defined in the present work. The He formation energy near the W(100) surface roughly increases with depth and converges to the bulk value of 6.2 eV at a depth of about 0.6 nm; however, the He interstitial at different depths below the W(110) surface has similar formation energies. The TM phenomenon was observed in the DFT calculations for He at the initial TISs near the 4th and 5th layers below the W(111) surface, which is consistent with the result

TABLE IV. Formation energy (eV) of He<sub>2</sub>V at different layers below W surfaces. \* indicates that no stable configuration was observed, and the helium desorbed.

Structure	L1	L2	L3	L4	L5	L6	L7	L8	L9	L10
W(100)	*	*	7.63	8.11	7.95	8.00	7.94			
W(110)	*	7.45	7.72	7.97	7.93	7.97				
W(111)	*	*	*	8.22	8.19	8.00	8.02	7.88	7.99	8.04

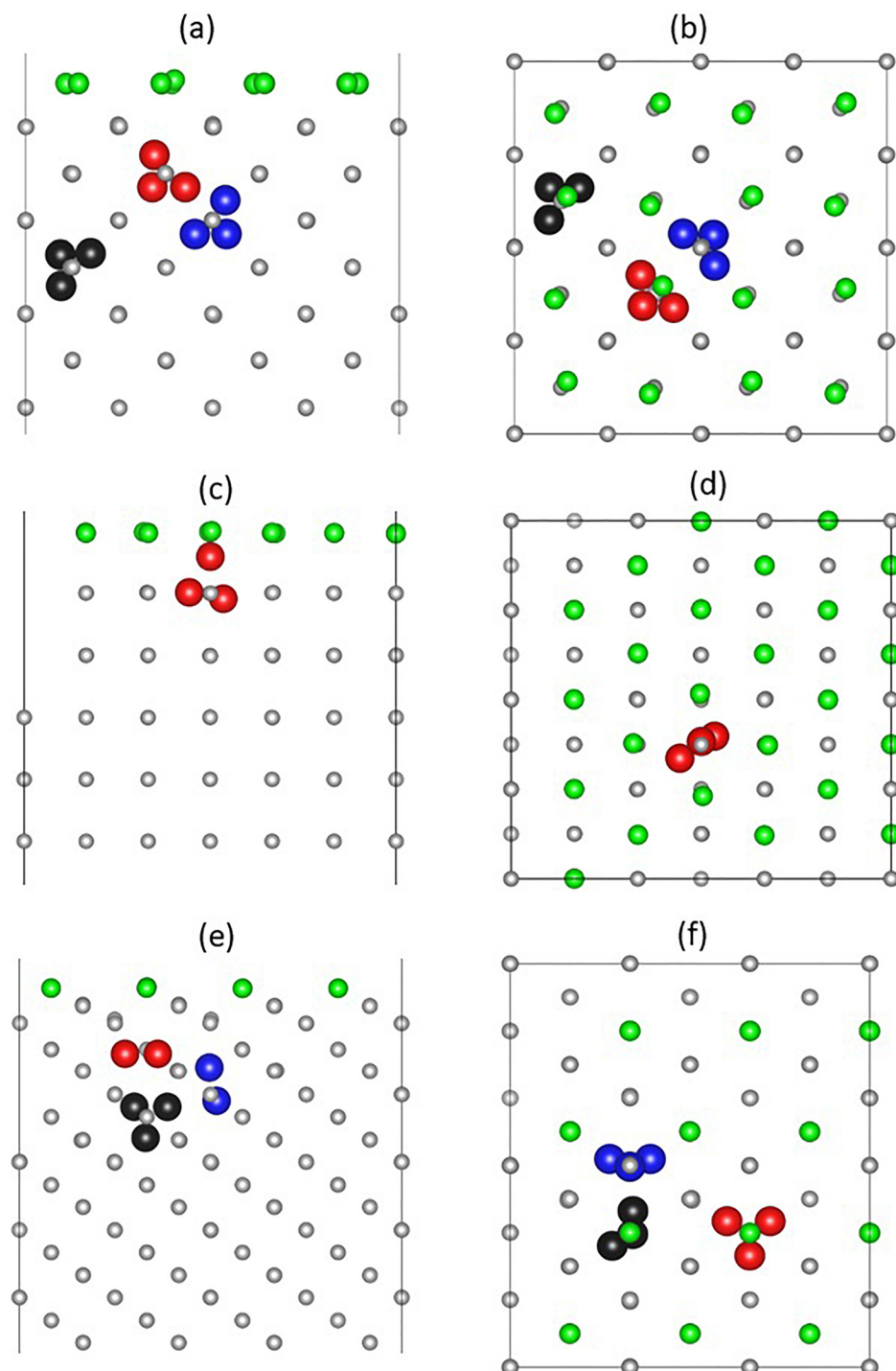


FIG. 7. Configurations of the stable He<sub>3</sub>V as viewed from the (a) side and (b) top of the W(100) surface; (c) side and (d) top of the W(110) surface; and the (e) side and (f) top of the W(111) surface. The representations of the symbols and the views are the same as those in Fig. 5.

in Ref. 25. Moreover, the present results indicate that the He formation energy remains almost constant at depths beyond 0.6 nm below the W(111) surface, which is not found in Ref. 25, presumably due to the small model used in Ref. 25.

TABLE V. Formation energy (eV) of He<sub>3</sub>V at different layers below W surfaces. The representation of \* is the same as that in Table IV.

Structure	L1	L2	L3	L4	L5	L6	L7	L8	L9	L10
W(100)	*	*	10.71	11.21	11.05	11.07	11.03			
W(110)	*	10.68	10.83	11.06	11.04	11.03				
W(111)	*	*	*	11.26	10.99	11.00	11.03	10.90	11.06	11.08

However, the He formation energy at different surfaces exhibits the same order as that in Ref. 25, i.e., the He formation energy is the lowest near the W(111), followed by the W(100) and W(110) surfaces.

Based on the formation energies of He and He<sub>m</sub>V ( $m=0, 1, 2$ ), the binding energy of He to a single vacancy, HeV, and He<sub>2</sub>V was obtained and is shown in Fig. 10. In bulk W, the binding energy of He to a vacancy, HeV, and He<sub>2</sub>V is 4.56, 3.11, and 3.12 eV, respectively, which are comparable to previous DFT and MD results.<sup>41,42</sup> As discussed above, the two top layers of the W(100) surface cannot trap He. From the 3rd layer ( $d=0.307$  nm) to the 6th layer ( $d=0.623$  nm) below the W(100) surface, the binding

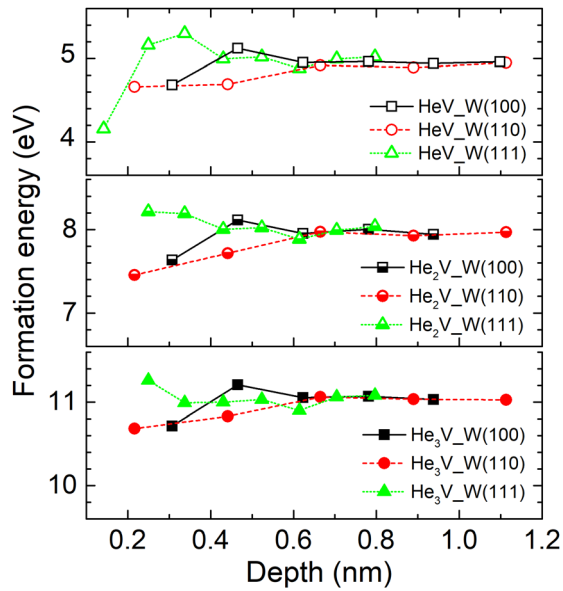


FIG. 8. Formation energies of  $\text{He}_m\text{V}$  ( $m=1, 2, 3$ ) as a function of depth below the W(100), W(110), and W(111) surfaces, respectively.

energies of He to  $\text{He}_m\text{V}$  complexes ( $m=0, 1, 2$ ) decrease with proximity to the surface, but approach a constant value beyond a depth of 6 layers. For the case of the W(110) surface, from the 2nd layer ( $d=0.216$  nm) to the 3rd layer ( $d=0.441$  nm), the binding energy of He to both a single vacancy and a  $\text{He}_2\text{V}$  complex increases and then reaches the bulk value for depths beyond the 3rd layer [see Figs. 10(a) and 10(c)]. However, the additional He trapping by a  $\text{HeV}$  at the W(110) surface is similar from the 2nd to 6th layers, as shown in Fig. 10(b). The binding energies of He to a vacancy below the W(111) surface indicate that the vacancies at the 3rd ( $d=0.14$  nm) and 4th layers ( $d=0.25$  nm) below the W(111) surface can weakly trap a He with a low He binding energy. After the trapping of the first He by the vacancy, the He trapping ability of the He-V complexes near the three W

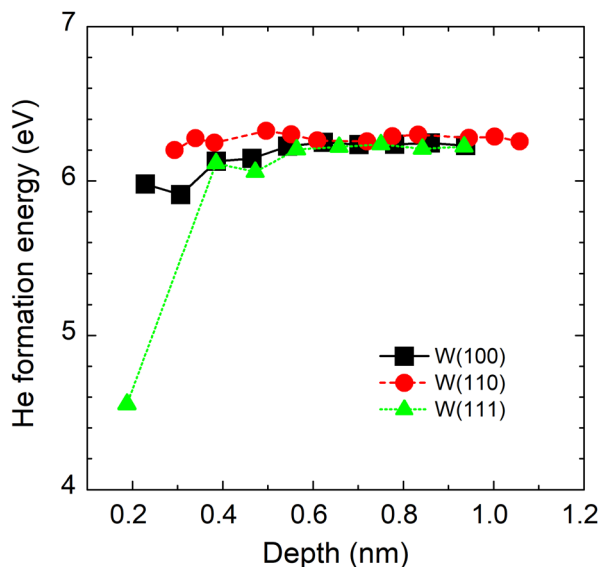


FIG. 9. Formation energies of He interstitial as a function of depth below the W(100), W(110), and W(111) surfaces.

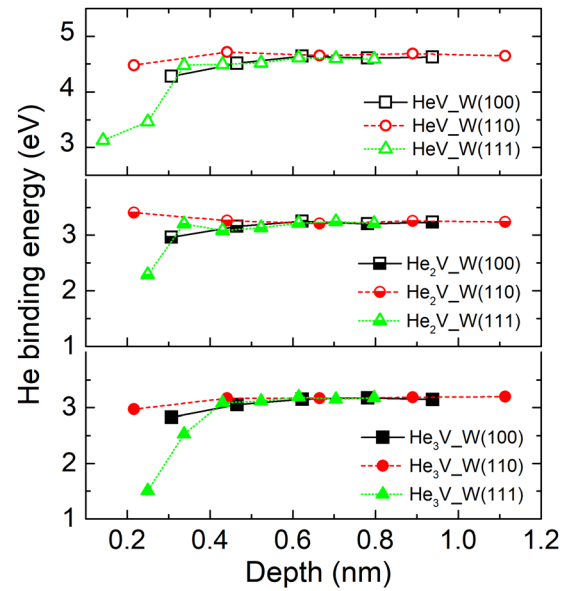


FIG. 10. Binding energies of He to (a) V, (b)  $\text{HeV}$ , and (c)  $\text{He}_2\text{V}$  as a function of depth below the W(100), W(110), and W(111) surfaces, respectively.

surfaces decreases [see Figs. 10(a) and 10(b)]. However, the binding energies of He to  $\text{HeV}$  complexes are almost the same as that of He to  $\text{He}_2\text{V}$  complexes at the same depth below the W(100), as illustrated in Figs. 10(b) and 10(c). It is of interest to note that He binding energy to He-V complexes decreases with increasing He concentration near the W(111) surface. Comparing the three W surfaces, the He has the highest binding energy to a vacancy below the W(110) surface.

## 2. $\text{He}_m\text{V}_2$ ( $m=1, 2, 3$ )

In order to obtain insight into the effect of the size of the He-V complex on He trapping near W surfaces, the formation energies of  $\text{He}_m\text{V}_2$  ( $m=1, 2, 3$ ) based on the stable  $\text{V}_{2-1\text{NN}}$  near the W(100), W(110), and W(111) surface were determined, as shown in Fig. 11. As illustrated in Fig. 2, the low formation energies of di-vacancies at depths less than 0.2 nm below the three W surfaces suggest that the di-vacancies at the corresponding region are easily created, but those di-vacancies cannot trap He. The  $\text{HeV}_2$  at a depth of 0.228 nm (the two vacancies occupy the 2nd and 3rd layers) below the W(100) surface has the second lowest formation energy of 6.25 eV, as shown in Fig. 11(a). The He at the  $\text{V}_2$  in bulk W is located at the center of the  $\text{V}_{2-1\text{NN}}$ . However, the vacancy at the 2nd layer of the W(100) surface is squeezed by the atoms of the top layer, which induces the movement of He towards the vacancy at the 3rd layer. The di-vacancies at a depth of 0.217 nm (the 2nd layer) below the W(110) surface can trap He, forming stable  $\text{HeV}_2$  with the formation energy of 7.71 eV. Unlike the monotonic increase in the di-vacancy formation energy with increasing depth near the W(110) surface (see Fig. 2), the formation energy of  $\text{HeV}_2$  at  $d=0.284$  nm (2nd-3rd layers) below the W(110) surface is the lowest. It is expected that the He at the di-vacancy would like the vacancy at the 2nd layer due to the attraction of the surface. On the contrary, the He at the

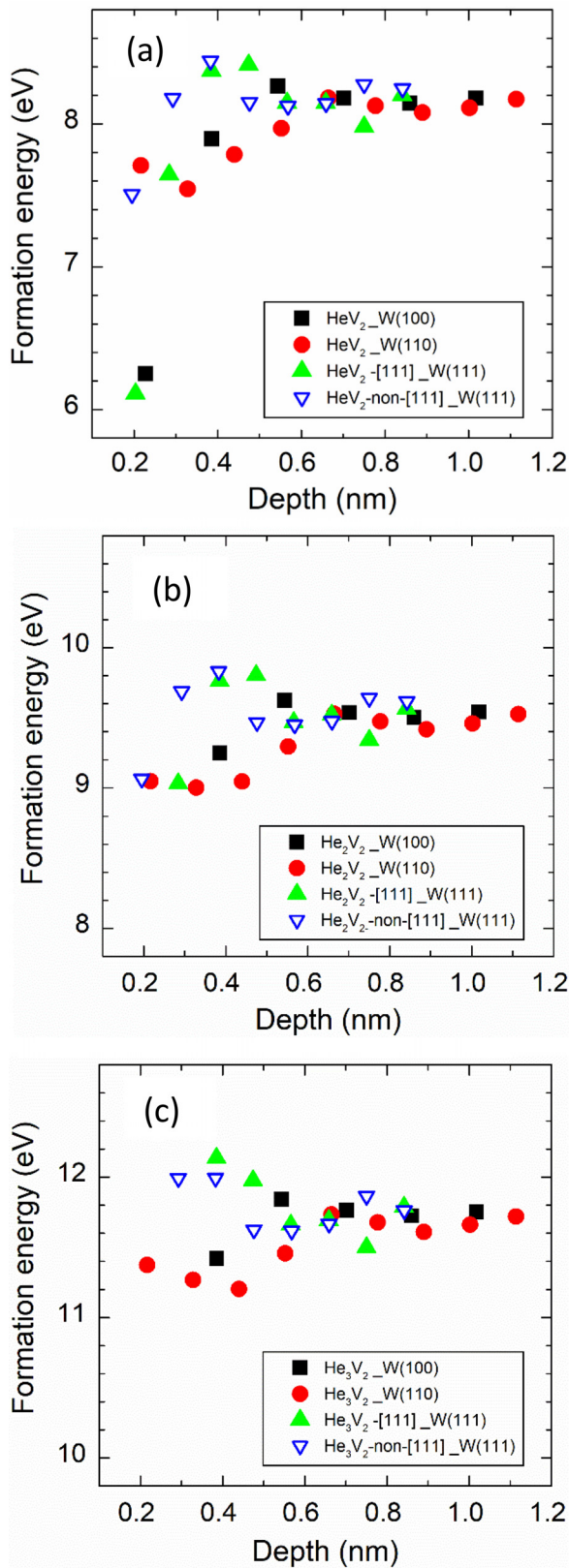


FIG. 11. Formation energies of (a) HeV<sub>2</sub>, (b) He<sub>2</sub>V<sub>2</sub>, and (c) He<sub>3</sub>V<sub>2</sub> as a function of depth below the W(100), W(110), and W(111) surfaces, where the representations of the symbols are similar to those in Fig. 2.

di-vacancy would rather occupy the vacancy at the 3rd layer than the vacancy at the 2nd layer. Similar to the formation energies of the V<sub>2-1NN</sub> near the W(111) surface, the formation energies of the HeV<sub>2</sub> along the [111] direction between

0.2 and 0.4 nm are much lower than that of the non-[111] directions, which indicates that the HeV<sub>2</sub> would like to be perpendicular to the (111) surface. Furthermore, like the HeV<sub>2-1NN</sub> at the 2nd-3rd layers below the W(100) and W(110) surfaces, the He at the di-vacancies along the [111] direction at  $d=0.2-0.4$  nm and the He at the di-vacancy along the non-[111] direction at  $d=0.293$  nm (the 4th-5th layers) would like to occupy the further vacancy from the surface layer. Comparing the formation energies of HeV<sub>2</sub> below the three W surfaces, it can be observed that the formation energy of HeV<sub>2</sub> at a depth of about 0.2 nm below the W(110) surface is larger than that below the W(111) and W(100) surfaces, whereas for depths from 0.3 to 0.6 nm below the W(110) surface, the formation energy is lower than the other two surfaces. Beyond 0.6 nm, the formation energy of HeV<sub>2</sub> is close to the bulk value of 8.18 eV. The trend of the formation energy of HeV<sub>2</sub> with depths is similar to that of di-vacancies near the three W surfaces.

Although the V<sub>2-1NN</sub> at  $d=0.228$  nm (the 2nd-3rd layers) below the W(100) surface can trap one He, no more He can be trapped by this di-vacancy. Once a He comes to this HeV<sub>2</sub>, a He<sub>2</sub>V<sub>2</sub> is temporarily formed, but is unstable in the current calculations. The He closest to the surface in the He<sub>2</sub>V<sub>2</sub> detraps from the vacancies, followed by the second, and both He desorb from the W(100) surface. The He<sub>2</sub>V<sub>2</sub> cluster along the [111] direction at a depth of about 0.2 nm below the W(111) surface is also unstable and becomes a HeV<sub>2</sub> due to the escape of the He closest to the surface. Figure 11(b) indicates that the formation energies of He<sub>2</sub>V<sub>2</sub> near the W(110) surface are the lowest and then followed by the W(100) and W(111) surfaces.

In terms of the growth of He<sub>m</sub>V<sub>2</sub> complexes, the He<sub>3</sub>V<sub>2</sub> cluster at depths of 0.2–0.55 nm below the W(110) surface and at a depth of 0.386 nm below the W(100) surface is stable, but this cluster is unstable along the non-[111] direction at 0.204 nm and along the [111] direction at 0.285 nm below the W(111) surface. Although the [111] di-vacancy at 0.285 nm can trap two He with the formation energy of 9.1 eV, once an additional He joins the cluster, an unstable He<sub>3</sub>V<sub>2</sub> cluster is the result. This He<sub>3</sub>V<sub>2</sub> configuration becomes a HeV<sub>2</sub> due to the detrapping of two He, which desorb from the surface. Figure 11 shows that with increasing number of He, the formation energies of He<sub>m</sub>V<sub>2</sub> at depths of 0.2–0.55 nm below the W(110) surface are obviously lower than those at the same depth below the W(100) and W(111) surfaces, especially for the He<sub>3</sub>V<sub>2</sub>. The formation energies of He<sub>m</sub>V below the W(100), W(110), and W(111) surfaces converge to bulk values at a depth of about 0.65 nm (see Fig. 8). The slightly larger formation energy of the He<sub>m</sub>V<sub>2</sub> cluster below the W(100) and W(110) surfaces converge to bulk values at depths of about 0.7 nm, while the formation energies of He<sub>m</sub>V<sub>2</sub> complexes below the W(111) surface appear to fluctuate until depths larger than 0.8 nm. With increasing number of He at the di-vacancy, the trend of the formation energy of He<sub>m</sub>V<sub>2</sub> with depths generally remains the same for the W(100) and W(111) surfaces, while different for the W(110) surface, especially at a depth of about 0.4 nm.

The binding energies of He to He<sub>m</sub>V<sub>2</sub> complexes ( $m=0, 1, 2$ ) below the W(100), W(110), and W(111)

surfaces are plotted in Fig. 12. Below the W(100) surface, the binding energy of He to the di-vacancy increases slightly with depths until the depth is about 0.65 nm. However, beyond 0.3 nm, the binding energy of He to a di-vacancy

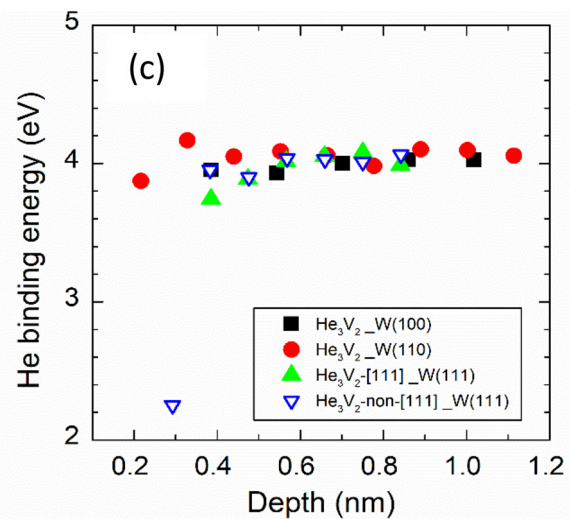
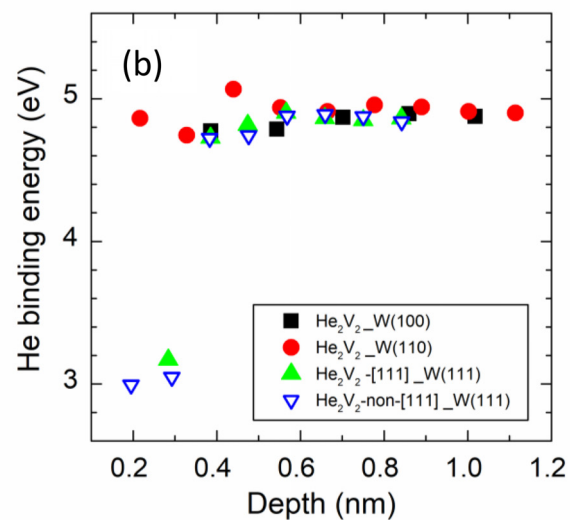
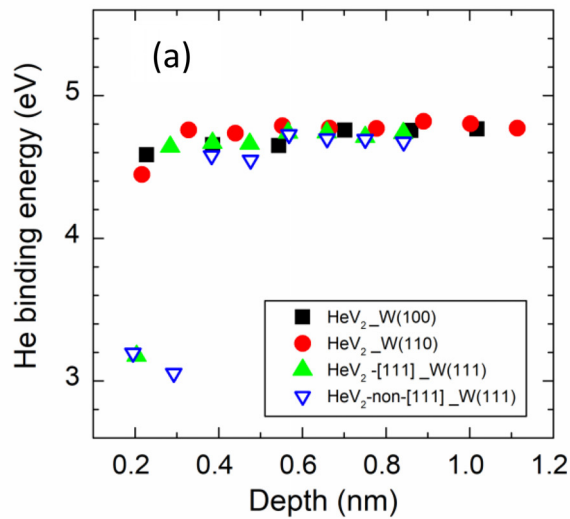


FIG. 12. Binding energies of He to (a)  $V_2$ , (b)  $HeV_2$ , and (c)  $He_2V_2$  as a function of depth below the W(100), W(110), and W(111) surfaces, where the representations of the symbols are the same as those in Fig. 11.

below the W(110) surface is close to the bulk result. It is of interest to note that the  $HeV_2$  complexes along the [111] direction below the W(111) surface have significant lower formation energies [see Fig. 11(a)], and thus generally higher He binding energies than that along the non-[111] directions [see Fig. 12(a)]. It is clear that the binding energies of He to a di-vacancy near the W(111) surface are substantially lower than that of the other two surfaces at depths of around 0.2–0.3 nm. At deeper depths, the binding energies of He to a di-vacancy below the W(110) surface are slightly larger than both the W(100) and W(111) surfaces. Beyond the depth of about 0.65 nm, the binding energy of He to a di-vacancy for each of the three W surfaces is close to the bulk value of 4.71 eV, as illustrated in Fig. 12(a).

At depths less than 0.38 nm, the  $He_2V_2$  near the W(100) surface and the  $He_2V_2$  along the [111] direction near the W(111) surface are unstable, and the binding energies of He to the  $HeV$  below the W(110) surface are obviously larger than below the W(111) surface. At depths deeper than 0.65 nm, the binding energies of He to  $HeV_2$  complexes are similar to the bulk value of 4.83 eV for the three W surfaces, as shown in Fig. 12(b). With the trapping of the third He at the  $V_{2-1NN}$  in bulk W, the He binding energy of  $He_3V_2$  decreases to 3.96 eV. Obviously, the binding energy of He to a  $He_2V_2$  near the W surface increases with depth and then approaches the bulk value as the depth is larger than 0.65 nm, as shown in Fig. 12(c). With increasing number of He, the  $He_mV_2$  complexes along the [111] direction near the W(111) surface become more unstable than that along the non-[111] directions. It is important to note that the He binding energies to  $He_mV_2$  ( $m=0, 1, 2$ ) complexes below the W(110) surface are generally higher than below the W(100) and W(111) surfaces.

In summary, the near surface region below each of the three W surfaces can be divided into three regions when describing the He trapping. In region I, with a depth  $< d_1$ , perfect surfaces and the vacancies near the three W surfaces cannot trap He, as shown in Figs. 8–12. In region II, with depths between  $d_1$  and  $d_2$ , the interstitial He prefers to stay below the perfect W(111) surface with a lower formation energy relative to the perfect W(100) or W(110) surfaces, as shown in Fig. 9. Generally, within region II, the formation energies of He-V complexes below the W(110) surface are lower than the W(100) and W(111) surfaces (see Figs. 8 and 11), and correspondingly, the binding energies of He to He-V complexes below the W(110) surface are higher than the W(100) and W(111) surfaces (see Figs. 10 and 12), which suggest that the vacancies below the W(110) surface can trap more He than W(100) and W(111) surfaces. Region III occurs at depths larger than  $d_2$ , in which the behavior of He-V complexes below the surfaces is similar to that in the bulk. The values of  $d_1$  and  $d_2$  increase with the size of the He-V complexes. For the small complexes considered in this work, the  $d_1$  and  $d_2$  are about 0.2 nm and 0.65–0.8 nm, respectively. Besides the lower formation energies of He-V complexes and higher binding energies of He to He-V complexes below the W(110) surface than that below the W(100) and W(111) surfaces, it is important to note that for the He content investigated, an increase in He concentration of the  $He_mV_n$

clusters de-stabilized the cluster below the W(100) and W(111) surfaces, but not below the W(110) surface. This indicates a higher He trapping ability by vacancies below the W(110) surface, which may imply that the size and density of He bubbles below the W(110) surface could be larger and lower than the other two W surfaces, respectively. The inference based on the present DFT results is somewhat consistent with the experimental phenomenon of the initial differences in surface morphology changes observed in (100) and (110) single crystal W samples under He plasma irradiation at low fluence,<sup>20</sup> and is in agreement with the experimental results that the density of He bubbles below the W(110) surface is less than the W(100) case.<sup>20</sup>

#### IV. CONCLUSION

In the present work, the stability of  $\text{He}_m\text{V}_n$  ( $m=0, 1, 2, 3$  and  $n=1, 2$ ) complexes below the W(100), W(110), and W(111) surfaces has been investigated by analyzing the formation and binding energies of  $\text{He}_m\text{V}_n$  complexes, which were obtained by DFT calculations using VASP. The results show that near surface region below each of the three W surfaces can be divided into three regions when describing the stability of vacancies and He-V complexes. Within the first and second regions ( $d < 0.65\text{--}0.8\text{ nm}$ ), the stability of vacancies and He-V complexes varies strongly and depends on the W surface orientation. However, in the third region ( $d > 0.65\text{--}0.8\text{ nm}$ ), the stability of the clusters is similar to the bulk. The formation energies of single vacancies and di-vacancies of the W(110) surface at the first region ( $d < 0.2$ ) are higher than that of the W(111) and W(100), which indicates higher stability of the surface layer of the W(110) surface. However, within the second near surface region ( $0.2\text{ nm} < d < 0.65\text{ nm}$ ), the formation energies of vacancies at the W(110) are lower than the other two W surfaces. In the third region ( $d > 0.65\text{ nm}$ ), the formation energy of vacancies is close to that in the bulk. The binding energy of a di-vacancy at the first layer of the W(110) surface is much higher than the other two W surface, but rapidly decreases to an unbound value beyond 0.2 nm. In general, the di-vacancy binding energies for the three W surfaces converge at depths greater than about 0.8 nm. The formation energies and He binding energies of He-V complexes are sensitive to both the He and vacancy configurations even at the same depth of a W surface, especially below the W(111) surface. Within the first near surface region of the three W surfaces, neither single vacancies nor di-vacancies can trap He. In the second region, the vacancies near the W(100) surface can trap more He than the W(100) and W(111) surfaces because of the lower formation energies of He-V complexes and higher binding energies of He to He-V complexes. Moreover, with increasing He concentration in the He-V complexes, the He desorption from the W(110) surface is less likely to occur than from the W(100) and W(111) surfaces.

#### ACKNOWLEDGMENTS

L. Yang and B. D. Wirth are grateful for partial support from the plasma surface interactions project of the Scientific Discovery through Advanced Computing (SciDAC)

program, which is jointly sponsored by the Fusion Energy Sciences (FES) and Advanced Scientific Computing Research (ASCR) programs within the U.S. Department of Energy Office of Science, as well as partial support by the Exascale Computing Project (17-SC-20-SC), a collaborative effort of the U.S. Department of Energy Office of Science and the National Nuclear Security Administration. Computing resources supporting the results presented in this manuscript were obtained at the National Energy Research Scientific Computing Center (NERSC), a DOE Office of Science User Facility supported by the Office of Science of the U.S. Department of Energy under Contract No. DE-AC02-05CH111231. ORNL is managed by UT-Battelle, LLC for the U.S. Department of Energy under Contract No. DE-AC05-00OR22725.

- <sup>1</sup>R. Causey, K. Kilson, T. Venhaus, and W. R. Wampler, *J. Nucl. Mater.* **266-269**, 467 (1999).
- <sup>2</sup>G. Federici, C. H. Skinner, J. N. Brooks *et al.*, *Nucl. Fusion* **41**, 1967 (2001).
- <sup>3</sup>S. Takamura, N. Ohno, D. Nishilima, and S. Kajita, *Plasma Fusion Res.* **1**, 051 (2006).
- <sup>4</sup>S. Kajita, W. Sakaguchi, N. Ohno, N. Yoshida, and T. Saeki, *Nucl. Fusion* **49**, 095005 (2009).
- <sup>5</sup>K. R. Umstadter, R. Doerner, and G. Tynan, *J. Nucl. Mater.* **386-388**, 751 (2009).
- <sup>6</sup>W. M. Shu, E. Wakai, and T. Yamnaishi, *Nucl. Fusion* **47**, 201 (2007).
- <sup>7</sup>M. J. Baldwin and R. P. Doerner, *Nucl. Fusion* **48**, 035001 (2008).
- <sup>8</sup>P. Fifiis, D. Curreli, and D. N. Ruzic, *Nucl. Fusion* **55**, 033020 (2015).
- <sup>9</sup>D. Maroudas, S. Blondel, L. Hu, K. D. Hammond, and B. D. Wirth, *J. Phys.: Condens. Matter* **28**, 064004 (2016).
- <sup>10</sup>A. M. Ito, A. Takayama, Y. Oda *et al.*, *Nucl. Fusion* **55**, 073013 (2015).
- <sup>11</sup>S. I. Krasheninnikov, *Phys. Scr. T* **145**, 014040 (2011).
- <sup>12</sup>Yu. V. Martynenko and M. Yu. Nagel, *Plasma Phys. Rep.* **38**, 996 (2012).
- <sup>13</sup>A. Lasa, S. K. Tahtinen, and K. Nordlund, *Europhys. Lett.* **105**, 25002 (2014).
- <sup>14</sup>K. Wang, R. P. Doerner, M. J. Baldwin, F. W. Meyer, M. E. Bannister, A. Darbal, R. Stroud, and C. M. Parish, *Sci. Rep.* **7**, 42315 (2017).
- <sup>15</sup>D. Nishijima, M. Miyamoto, H. Iwakiri, M. Ye, N. Ohno, K. Tokunaga, N. Yoshida, and S. Takamura, *Mater. Trans.* **46**, 561 (2005).
- <sup>16</sup>H. B. Zhou, Y. L. Liu, and G. H. Lu, *Comput. Mater. Sci.* **112**, 487 (2016).
- <sup>17</sup>M. Yamagiwa, S. Kajita, N. Ohno, M. Takagi, N. Yoshida, R. Yoshihara, W. Sakaguchi, and H. Kurishita, *J. Nucl. Mater.* **417**, 499 (2011).
- <sup>18</sup>N. Ohno, Y. Hirahata, M. Yamagiwa, S. Kajita, M. Takagi, N. Yoshida, R. Yoshihara, T. Tokunaga, and M. Tokitani, *J. Nucl. Mater.* **438**, S879 (2013).
- <sup>19</sup>C. M. Parish, H. Hijazi, H. M. Meyer, and F. W. Meyer, *Acta Materialia* **62**, 173 (2014).
- <sup>20</sup>S. Kajita, N. Yoshida, N. Ohno, Y. Hirahata, and R. Yoshihara, *Phys. Scr.* **89**, 025602 (2014).
- <sup>21</sup>W. D. Wilson, C. L. Bisson, and M. I. Baskes, *Phys. Rev. B* **24**, 5616 (1981).
- <sup>22</sup>L. Hu, K. D. Hammond, B. D. Wirth, and D. Maroudas, *J. Appl. Phys.* **118**, 163301 (2015).
- <sup>23</sup>F. Sefta, K. D. Hammond, N. Juslin, and B. D. Wirth, *Nucl. Fusion* **53**, 073015 (2013).
- <sup>24</sup>J. L. Wang, Y. Zhang, H. B. Zhou, S. Jin, and G. H. Lu, *J. Nucl. Mater.* **461**, 230 (2015).
- <sup>25</sup>G. Y. Pan, Y. G. Li, Y. S. Zhang, C. G. Zhang, Z. Zhao, and Z. Zeng, *RSC Adv.* **7**, 25789 (2017).
- <sup>26</sup>G. Kresse and J. Furthmüller, *Comput. Mater. Sci.* **6**, 15 (1996).
- <sup>27</sup>G. Kresse and D. Joubert, *Phys. Rev. B* **59**, 1758 (1999).
- <sup>28</sup>P. E. Blöchl, *Phys. Rev. B* **50**, 17953 (1994).
- <sup>29</sup>J. P. Perdew, K. Burke, and M. Ernzerhof, *Phys. Rev. Lett.* **77**, 3865 (1996).
- <sup>30</sup>D. Spišák and J. Hafner, *Phys. Rev. B* **70**, 195426 (2004).
- <sup>31</sup>K. D. Hammond and B. D. Wirth, *J. Appl. Phys.* **116**, 143301 (2014).
- <sup>32</sup>L. Sandoval, D. Perez, B. P. Uberuaga, and A. F. Voter, *Phys. Rev. Lett.* **114**, 105502 (2015).
- <sup>33</sup>L. Hu, K. D. Hammond, B. D. Wirth, and D. Maroudas, *J. Appl. Phys.* **115**, 173512 (2014).

- <sup>34</sup>G. Y. Huang, N. Juslin, and B. D. Wirth, *Comput. Mater. Sci.* **123**, 121 (2016).
- <sup>35</sup>G. D. Samolyuk, Y. N. Osetsky, and R. E. Stoller, *Fusion Sci. Technol.* **71**, 52 (2017).
- <sup>36</sup>C. S. Becquart and C. Domain, *Nucl. Instrum. Methods B* **255**, 23 (2007).
- <sup>37</sup>N. A. W. Holzwarth, J. A. Chervenak, C. J. Kimmer, Y. Zeng, W. Xu, and J. Adams, *Phys. Rev. B* **48**, 12136 (1993).
- <sup>38</sup>L. Yang, F. Gao, R. J. Kurtz, and X. T. Zu, *Acta Mater.* **82**, 275 (2015).
- <sup>39</sup>D. Perez, L. Sandoval, S. Blondel, B. D. Wirth, B. P. Uberuaga, and A. F. Voter, *Sci. Rep.* **7**, 2522 (2017).
- <sup>40</sup>Z. Zhao, Y. G. Li, C. G. Zhang, G. Y. Pan, P. F. Tang, and Z. Zeng, *Nucl. Fusion* **57**, 086020 (2017).
- <sup>41</sup>C. S. Becquart and C. Domain, *J. Nucl. Mater.* **385**, 223 (2009).
- <sup>42</sup>L. F. Wang, X. L. Shu, and G. H. Lu, *J. Mater. Res.* **30**, 1464 (2015).